FLOW CAMBRIDGE UNIVERSITY PRESS

RESEARCH ARTICLE

Unsteady flow behaviour of multi-rotors in ground proximity

Hasse N.J. Dekker[1,2,*] (ID), Woutijn J. Baars[1] (ID), Fulvio Scarano[1] (ID), Marthijn Tuinstra[2] and Daniele Ragni[1]

[1]Faculty of Aerospace Engineering, Delft University of Technology, Delft, 2629 HS, The Netherlands
[2]Royal Netherlands Aerospace Centre, Marknesse, 8316 PR, The Netherlands
*Corresponding author. E-mail: h.n.j.dekker-1@tudelft.nl

Abstract

The unsteady flow behaviour of two side-by-side rotors in ground proximity is experimentally investigated. The rotors induce a velocity distribution interacting with the ground causing the radial expansion of the rotor wakes. In between the rotors, an interaction of the two wakes takes place, resulting in an upward flow similar to a fountain. Two types of flow topologies are examined and correspond to two different stand-off heights between the rotors and the ground: the first one where the height of the fountain remains below the rotor disks, and a second one where it emerges above, being re-ingested. The fountain unsteadiness is shown to increase when re-ingestion takes place, determining a location switch from one rotor disk to the other, multiple times during acquisition. Consequently, variable inflow conditions are imposed on each of the two rotors. The fountain dynamics is observed at a frequency that is about two orders of magnitude lower than the blade passing frequency. The dominant characteristic time scale is linked to the flow recirculation path, relating this to system parameters of thrust and ground stand-off height. The flow field is analysed using proper orthogonal decomposition, in which coupled modes are identified. Results from the modal analysis are used to formulate a simple dynamic flow model of the re-ingestion switching cycle.

Impact Statement

Urban air mobility aims at a transportation system that will revolutionize travel times in metropolitan areas, by enabling air-linked destinations in closer proximity to one another than regular airports. Urban air mobility vehicles often employ multiple propulsors with a vertical take-off approach, to optimize versatility and manoeuvrability in confined environments. Multi-rotor systems operating in proximity to ground-based obstacles cause aerodynamic interactions which are detrimental to safety, aerodynamic performance and noise emissions. These interactions are often unpredictable, since they are influenced by velocity distributions in the rotor wakes, with very different time scales with respect to those of the rotor blades themselves. The time scales of a family of interactions of multi-rotor systems with ground surfaces are elucidated, relating these to system parameters of thrust and ground stand-off height.

1. Introduction

The emerging sector of urban air mobility (Garrow, German, & Leonard, 2021; Thipphavong et al., 2018) is leveraging electric vertical take-off and landing configurations, to deploy highly versatile
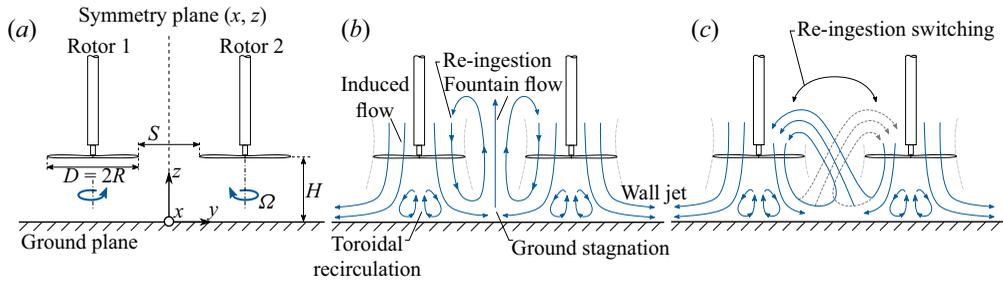
Figure 1. *(a) Schematic representation of the side-by-side rotor system in ground effect with relevant parameters and system of coordinates. (b) Conceptual flow topology. (c) Illustration of re-ingestion switching.*

and manoeuvrable disruptive aircraft systems. With the exception of a few configurations, the vertical flight phase of these future-generation vehicles is achieved through multiple rotors, to prioritize control and manoeuvrability. These rotors have an increased disk loading compared with single-rotor configurations (Rizzi et al., 2020). In the initial and final stages of the flight mission, the vehicle needs to hover in close proximity to the ground. In these conditions, axial momentum of the rotor's slipstream interacts with the ground plane. Such an interaction has been studied extensively for single rotors, both aerodynamically and aeroacoustically. A first known effect is the interaction between the slipstream and the ground producing stagnation below the rotor. This stagnation is most noticeable below the rotor hub, by the lower axial velocity in this region, which results in an axisymmetric separation region with toroidal recirculation (Fradenburgh, 1960). Aside from the stagnation region, the flow is rapidly redirected outwards along the wall, forming a radially spreading turbulent wall jet (Milluzzo & Leishman, 2017; Nathan & Green, 2012). A consequent aerodynamic change of performance is dictated by the adverse pressure gradient created by the ground, which determines a tip-speed ratio increase (when the rotor's rotation rate is held constant), along with the local blade angle and the blade loading (Cheeseman & Bennet, 1955; Fradenburgh, 1960).

Moving from the single-rotor to the multi-rotor system (see figure 1a), the axial asymmetry is no longer present and additional interactions between the rotor wakes occur. For very small rotor spacings S (tip-to-tip distance of approximately 5 % of the rotor radius), the slipstreams merge due to the Coandă effect (Zhou, Ning, Li, & Hu, 2017), before radial expansion takes place at the wall (Dekker, Ragni, Baars, Scarano, & Tuinstra, 2022). With increasing rotor spacing such merging does not occur. Instead, the radial wall jets formed at the ground collide along the symmetry plane between the rotors (Dekker et al., 2022; He & Leang, 2020). The adverse pressure gradient resulting from such a stagnation region causes the flow to separate from the ground and develop vertically upwards. The latter has been reported as fountain flow (Conyers, Rutherford, & Valavanis, 2018; He & Leang, 2020; Sanchez-Cuevas, Heredia, & Ollero, 2017), and is characterized by a pronounced unsteadiness due to the unstable behaviour of its relatively low speed and highly vortical front moving upward between the rotors. When the rotors are sufficiently close to the ground, the height of the fountain exceeds that of the rotors and the turbulent flow of the fountain is bent and re-ingested into the rotors (Conyers et al., 2018; Dekker et al., 2022; He & Leang, 2020), a condition schematically illustrated in figure 1(b). The rotor spacing S dictates the development of the fountain flow and the degree of re-ingestion (see figure 1a for relevant parameters). At small values of the rotor spacing ($S < 2R$) the fountain height decreases (Dekker et al., 2022) and for smaller rotor spacings this phenomenon disappears ($S \approx 0.1R$).

The effects of fountain flow re-ingestion on the system's performance are adverse. A recent study by He and Leang (2020) reports an 8 % drop in thrust $S = 2R$ and $H = 2R$, compared with the free-hover condition. Moreover, under these conditions the rotor is exposed to non-axial inflow conditions and ingests highly turbulent flow (Dekker et al., 2022). The latter results in unsteady blade loading and adversely affects thrust fluctuations, noise emissions (Wojno, Mueller, & Blake, 2002) and vibrations (as found recently from a numerical investigation by Healy, McCauley, Gandhi, Sahni, and Mistry (2021)).

The aforementioned studies focused upon the time-averaged effects of ground proximity, mainly to determine the steady flow field and pressure distribution around the system. Switching of the wake re-ingestion, multiple times from one rotor to the other, has been observed experimentally by Dekker et al. (2022), and was also noted in the numerical work of Healy et al. (2021). This switching cycle is illustrated in figure 1(*c*) by indicating the fountain region moving from side to side. When these are orientated near one of the two rotors, a sudden thrust deficit was observed, with the strength of vibrations increasing up to 10 % (Healy et al., 2021). The time scale associated with this lateral movement of the flow was found to be several orders of magnitude larger than that related to the rotational speed of the rotors (Dekker et al., 2022; Healy et al., 2021). It is therefore conjectured that the unsteadiness is not directly associated with the blade passages and the helical vortices trailing from the blade tips.

Several studies on interacting rotor flows have documented low-frequency unsteadiness within the flow field. For instance, the rotor–wing interaction of a tilt-rotor configuration in hover produces a fountain flow similar to that mentioned above, caused by the back pressure of the wing surface (Maisel, Giulanetti, & Dugan, 2000). In a study by Polak, Rehm, and George (2000) the effects of the fountain were isolated by the insertion of a physical plane, so-called image plane, between subsequent rotors. This effectively creates a half-span model and thus removed the interaction between the two rotor slipstreams. When the image plane was removed, the height of the fountain increased and it was shown to drift laterally resulting in 're-ingestion switching'. These results were also found in a numerical study by Zanotti, Savino, Palazzi, Tugnoli, and Muscarello (2021). The occurrence of this phenomenon is reported to be aperiodic (Polak et al., 2000) at a rate 1–2 orders of magnitude lower than the rotational frequency of the rotors (Potsdam & Strawn, 2005). The switching is believed to be responsible for an intermittent frequency in the acoustic spectrum of tilt-rotors in hover (Polak & George, 1998). Valuable observations of two interacting air columns are also made in studies concerning impinging jets, studied for the take-off aerodynamics of short take-off and vertical landing aircraft (Siclari, Migdal, Luzzi, Barche, & Palcza, 1976) as well as for a wide range of industrial applications (Huang & El-Genk, 1994). The location of a stagnation point in the foot of the fountain, between the jets, was shown to vary randomly in the lateral direction (Cabrita, Saddington, & Knowles, 2005; Saddington, Cabrita, & Knowles, 2005). Aside from this, variations in the emerging angle of the fountain plume from the wall have been observed (Stahl, Prasad, & Gaitonde, 2021).

A description of the spatial–temporal dynamics of the flow structures associated with the relatively large time scales of the unsteady flow field of side-by-side rotors in ground proximity is missing to date. Consequently, the relation between the geometric parameters and the aerodynamic performance remains unknown. Being able to predict such time scales as a function of the geometrical characteristics of the multi-rotor system allows one to predict the loss of performance and manoeuvrability issues and relate them to acoustic footprint changes. Hence, the present study starts with an instantaneous flow topology analysis, to bridge to the explanation of the effects of re-ingestion on the lateral dynamics of the fountain. Secondly, an attempt is made to identify the time scale of re-ingestion switching. Finally, a modal analysis is conducted to form a physical model between the geometrical flow path associated with and the time scales of re-ingestion switching and the convection of the flow itself.

The outline of the paper is as follows. Section 2 describes the experimental campaign on a side-by-side rotor system, forming the backbone of this study. In § 3, a description of the flow field is presented and the unsteady phenomenon of re-ingestion is introduced. In § 4, a proper orthogonal decomposition (POD) of the flow is conducted to discuss in detail the spatial and temporal properties of the flow. Finally, § 5 discusses the low-order representation of the flow dynamics.

2. Experimental apparatus and procedure

2.1. Side-by-side rotor system

Two counter-rotating rotors, separated by one rotor diameter from rotor tip to rotor tip, were installed with their axes perpendicular to a ground plane. Both rotors were two-bladed and comprised a radius

Table 1. *Side-by-side rotor operating conditions.*

|	
Blade passing frequency (Hz)	333
Number of blades B	2
Radius R (mm)	76.2
Blade chord c at 0.75R (mm)	11.2
Chord Reynolds number Re_c	42 000
Tip Mach number M_t	0.22
Lateral separation S/R (tip-to-tip)	2
Ground stand-off distance H/R (disk-to-ground)	[2, 4]
Out-of-ground effect thrust coefficient $C_t = T/(16\rho\Omega^2 R^4)$	0.117

$R = 76.2$ mm, with 4″ pitch and a parabolic tip. These are commercially available under model numbers APC 6X4E and APC 6X4EP (identical but mirrored, for the counter-rotating configuration). The ratio between the ground plane area and rotor disk area was approximately 35. Each rotor was driven by a geared in-runner brushless motor (Hacker, B20 26 L kv2020 + 4:1), at a shaft rotational speed of 167 Hz. Nominally, the blade passing frequency (BPF) was 333 Hz. No phase control between the rotors was present but this was monitored, together with the rotational speed, by using high-speed camera footage. From this followed a constant relative difference in rotational speed of less than 0.25 Hz over the acquisition duration of the measurement. The chord-based Reynolds number is $Re_c = 42\,000$ (with the chord taken at the 0.75R location) and the tip Mach number is $M_t = 0.22$. The rotors were operated with a thrust coefficient of $C_t = 0.117$ and provided $T = 2.14$ N of thrust, in the out-of-ground effect condition. Two different ground stand-off heights were considered during the experiment: $H/R = 2$ and $H/R = 4$. A summary of the operating conditions is presented in table 1.

2.2. Planar particle image velocimetry (PIV) measurements

Planar PIV measurements were acquired in the domain illustrated in figure 2. The experiment was conducted inside an enclosure of $2 \times 2 \times 3$ m^3 that confines the helium-filled soap bubbles (HFSB) used as flow tracers (Faleiros, Tuinstra, Sciacchitano, & Scarano, 2019). Any effects of re-circulation in the enclosure are observed at frequencies comparable to the BPF (Weitsman, Stephenson, & Zawodny, 2020) and therefore do not affect the relatively large time scales of interest. Five HFSB generators delivered roughly 150 000 bubbles per second, which were nearly neutrally buoyant and had a mean diameter of 0.4 mm. The enclosure was seeded for two minutes prior to performing the measurement, and resulted in a density of roughly 0.01 particles per pixel corresponding to a spatial concentration of 12 particles cm^{-2}. Laser illumination was provided by a Nd:YAG Continuum Mesa PIV 532-120-M laser. The laser beam was expanded by a cylindrical lens allowing a light sheet thickness of 2 cm. Its effective thickness was estimated using three-dimensional (3-D) flow data as 8 mm. The centre of the laser sheet was positioned with an offset of 1.5 cm from the rotor axes (in positive x direction) to avoid shadows from the rotor mounting. Illumination was given with a pulse width of $\delta t = 150$ ns and a rate of 4.0 kHz.

A high-speed CMOS camera (Photron Fastcam SA.5, 1024×1024 px^2) was used for imaging and placed outside the closed environment at a distance of 1 m from the measurement region. A lens with focal length $f = 50$ mm and a numerical aperture set to $f_\# = 8$ captured a field of view of 38.5×38.5 cm^2 ($5R \times 5R$) at a magnification of $M = 0.053$. Synchronization between the camera and the laser was obtained with a LaVision programmable timing unit (PTU X). Each experimental run captured 2.7 s of data (approximately 11 000 recordings) and was repeated six times, thus providing a total of roughly 16 s ($\approx$2750 rotor revolutions) of discontinuous measurements for each of the two configurations. Measurement parameters are summarized in table 2.

Two pre-processing steps were applied to the raw camera footage before computing PIV-based velocities. First, a minimum time filter was used to eliminate any stationary reflections from the ground
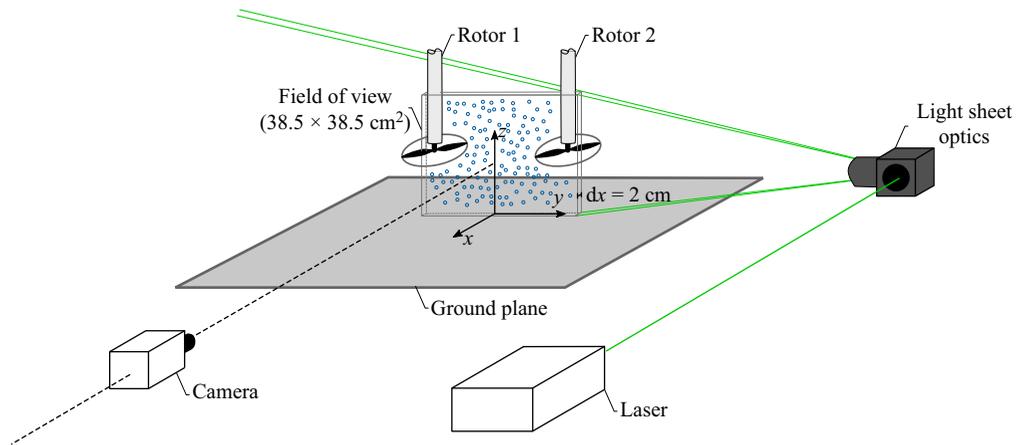
Figure 2. *A 3-D schematic of the experimental apparatus, coordinate system and measurement plane.*

Table 2. *Illumination and imaging conditions.*

Seeding type	HFSB
Seeding concentration (cm^{-2})	12
Illumination	Nd:YAG laser
Sheet thickness dx (cm)	2
Pulse width δt (ns)	150
Repetition rate (Hz)	4000
Camera type	Photron Fastcam SA.5 (1024×1024 px^2)
Objective focal length f (mm)	50
Numerical aperture $f_\#$	8
Optical magnification M	0.053
Field of view (cm^2)	38.5×38.5
Seeding density (particles px^{-1})	0.01
Number of recordings	$6 \times 10\,917$
Image analysis	Cross-correlation (24×24 px^2)

plane and support struts of the rotors. Second, a sliding minimum filter with a length scale of 3 pixels was applied to reduce any unsteady rotor-blade reflections. Planar velocity components were inferred by cross-correlation between subsequent images, with a window size of 24×24 px^2 and an overlap of 75 %. This resulted in a vector resolution of 8 mm and a vector spacing of 2 mm. The velocity field was then cropped to a physical domain of 31×27 cm^2. As a final post-processing step, time super-sampling with a factor of 5 was applied to improve the quality of the velocity spectra.

The measurement uncertainty ϵ_w for the instantaneous velocity field was computed using the method of correlation statistics as described by Wieneke (2015). Values of ϵ_w were compared to the induced velocity of a single rotor without a ground plane ($w_{ind} = 14.25$ m s^{-1}). From this follows an average instantaneous uncertainty of approximately 4 % of the rotor-induced velocity. Conclusions drawn from these data on the large-scale flow dynamics are not affected by this relatively small uncertainty.

2.3. The 3-D dataset

Supplementary to the described experiments, the current work also makes use of a previously performed experiment, where the flow field was measured in a 3-D domain (see Dekker et al., 2022). Such data, although encompassing a shorter observation time (1 s in total), bring additional information on the

instantaneous flow organization. A short summary of the Dekker et al. (2022) dataset is provided here. The HFSB were illuminated by a LaVision LED-Flashlight 300 device in a volume spanning $20 \times 31 \times 33$ cm^3. A tomographic imaging set-up comprised three high-speed CMOS cameras (Photron Fastcam SA1.1). Each measurement included 2000 image recordings at a rate of 2.0 kHz. The 3-D particle motion analysis was performed with the 'shake-the-box' method (Schanz, Gesemann, & Schröder, 2016). This delivered approximately 10 000 particle tracks for each time step with a maximum particle displacement of 20 pixels (a physical displacement of 6.4 mm). The instantaneous velocity field was reconstructed using the vortex-in-cell technique (VIC+) as described by Schneiders and Scarano (2016) for 3-D scattered particle data; calculations were done in DaVis, with the modified algorithm VIC# (Jeon, Müller, Michaelis, & Wieneke, 2018). The instantaneous velocity field was reconstructed on a grid with $h = 3.8$ mm spacing between neighbouring vectors.

3. Flow-field analysis

3.1. Three-dimensional flow topology

Observations of the unsteady flow behaviour of the multi-rotor system in ground proximity, based on the instantaneous and mean flow fields, are described in this section. An illustration of the fountain phenomenon is shown in figure 3(*a*), for a ground stand-off distance of four radii. Shown are the instantaneous velocity magnitude (blue) and positive axial velocity iso-surfaces (red); the velocity has been normalized by w_{ind} and is adopted for all results displaying normalized velocity.

In figure 3(*a*), the rotor slipstreams develop two wall jets that stagnate near the ground plane. The collision of these jets along the stagnation line between the rotors results in the fountain flow, highlighted by the red iso-surfaces, and reaches up to three rotor radii in height. When the ground stand-off distance is reduced to two rotor radii, the fountain remains similar in height (figure 3*b*) by the balance between the increase of stagnation pressure with reduced height (for constant thrust) and the reduced inflow to the rotor by the presence of the ground. In this case, the fountain reaches above the rotor disk and is inclined towards the left-sided rotor 1. Furthermore, the toroidal separation region in the centre of the wake has increased, as is particularly visible in the wake of rotor 2 not being affected by a re-ingestion. The rotor wake involves tip/root vortices of the blades, as well as the blade section wakes. Due to the relatively high loading in the hover scenario, the tip vortices are the dominant flow features carried to the fountain where they are ejected from the ground. This is confirmed by computing the λ_2-criterion, which is visualized for both ground stand-off distances in figures 3(*c*) and 3(*d*). In figure 3(*c*), the path of the blade tip vortices is clearly visible close to the blade. They are visible for wake ages up to three to four rotor revolutions before breakdown occurs. Even though the helical structure of the wake is lost after this, coherent structures are still present close to the ground and even within the upward fountain flow. A different phenomenon is present in figure 3(*d*) for $H/R = 2$, where the wake expands before the vortices break down. Consequently, the vorticity is increased by vortex stretching, similar to what is found for a single rotor in ground proximity (Lee, Leishman, & Ramasamy, 2010). This is likely to be the reason why larger vortex structures are present in the fountain for the lower ground stand-off distance. Furthermore, since the fountain reached above the rotor disk, coherent structures get re-ingested into rotor 1 (at the time instant of the instantaneous field in figure 3*d*). Note that the direction of re-ingestion was observed changing back and forth from rotor 1 to rotor 2. This re-ingestion switching occurred at a relatively large time scale, in comparison to 1 s acquisition period of the 3-D data. In order to further focus on the plane of the fountain switching, we proceed with the two-dimensional (2-D) dataset for a more detailed analysis of the velocity distribution. The choice to switch to planar velocimetry data is justified by the limited out-of-plane motions in the fountain plume. On a final note, the two different flow topologies presented in this section were found for constant thrust coefficient C_t. Since the height of the fountain is proportional to the induced velocity of the rotors and therefore to the thrust coefficient, it is expected that the minimal ground stand-off height H/R for re-ingestion to occur decreases with increasing thrust.
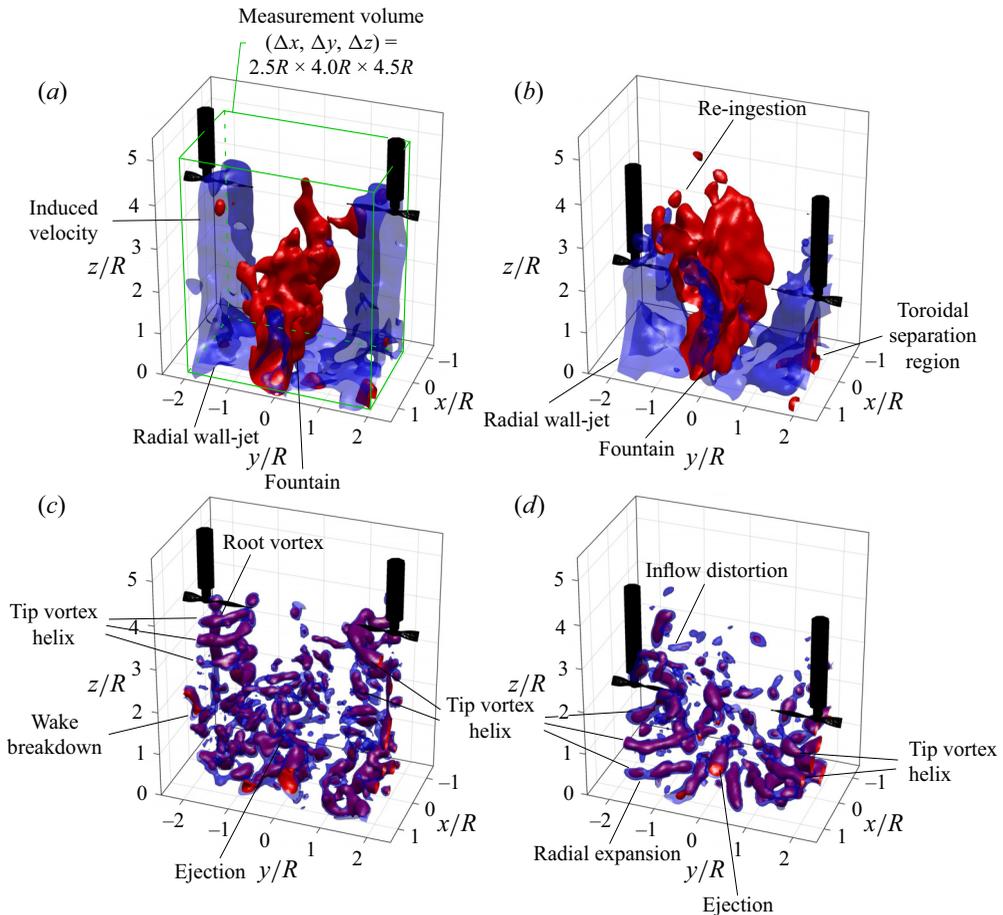
Figure 3. *Iso-surfaces of normalized velocity magnitude $V/w_{ind} = 0.5$ (blue) and $w/w_{ind} = 0.25$ (red) for (a) $H/R = 4$ and (b) $H/R = 2$. Iso-surfaces of $\lambda_2 = -60\,000$ s^2 (blue) and $\lambda_2 = -90\,000$ s^2 (red) for (c) $H/R = 4$ and (d) $H/R = 2$. The measurement volume is illustrated by the green box in (a).*

### 3.2. Velocity field statistics

In the previous section, an asymmetric re-ingestion was noted on the basis of an instantaneous velocity field. This asymmetry is also noticeable in the time-averaged results of the 2-D velocity measurements, as evidenced by the axial velocity contours and velocity streamlines in figure 4.

For a rotor height of four rotor radii in figure 4(a), the upward fountain flow is inclined towards the slipstream of rotor 1. Effects of the fountain flow inclination are visible throughout the domain: a missing toroidal separation region for the wake where the fountain is inclined towards (compare points A and B), and furthermore, a nodal point, n_1, appears near the fountain and highlights the entrainment of air to the fountain (Cabrita et al., 2005). When the rotor ground stand-off distance is reduced to two rotor radii (figure 4b), the fountain flow reaches above the rotor disk, after which it is re-ingested. In figure 4(b), two nodal points n_2 and n_3 are found with a slight offset in height, and the fountain is inclined towards the side with the lower nodal point. Ultimately, this affects the wake distribution, where rotor 1 has more momentum in the centre of the wake. As for figure 4(a), the toroidal separation regions are also affected in an asymmetric manner (points C and D).

The root mean square of the axial and lateral velocity fluctuations are presented in figure 5 for both ground stand-off distances. In the axial direction, the most intense fluctuations are found in the
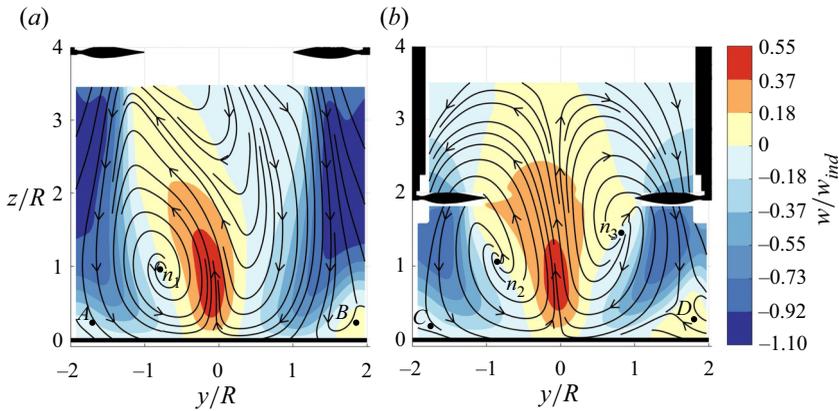
Figure 4. *Time-averaged axial velocity contours and 2-D streamlines computed over one acquisition (2.7 s) for (a) H/R = 4 and (b) H/R = 2. Annotations n_1, n_2 and n_3 denote nodal points in the domain.*
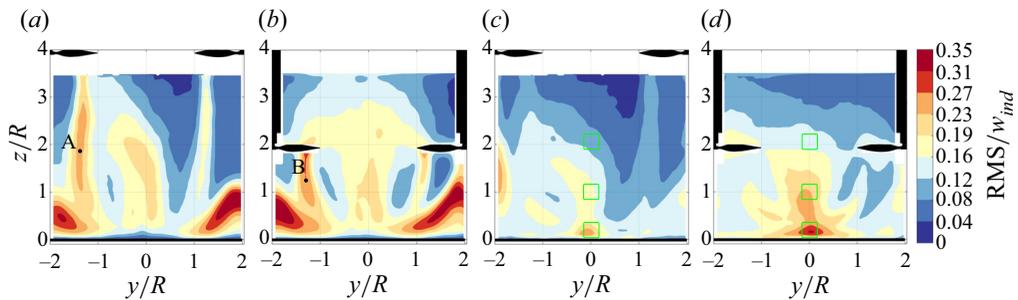

Figure 5. *Root mean square of velocity fluctuation in axial direction for (a) H/R = 2 and (b) H/R = 4, and in lateral direction for (c) H/R = 2 and (d) H/R = 4. Green rectangles denote the regions where the vectors are extracted for generating figure 6.*

separation regions below each rotor (see figures 5a and 5b). The fluctuations are also intense along the boundaries of the slipstream, caused by the tip vortices (see points A and B in these figures). Moreover, the fluctuations are stronger in the slipstream of the rotor that re-ingests the fountain flow, which is expected due to the turbulence ingestion. The strongest fluctuations in the lateral direction are found in the stagnation points near the ground (figures 5c and 5d). For the lower rotor ground stand-off distance, the fluctuations comprise a larger magnitude and exhibit a larger extent into the fountain flow.

3.3. Fountain flow dynamics

In order to examine the relation between the fountain flow unsteadiness and the BPF, the pre-multiplied spectrum of the lateral velocity fluctuations is computed, at different heights within the fountain. For the calculation of the spectra, roughly 330 000 samples are collected. These are divided into ensembles of 2^{13} samples and processed using the Welch method (50 % overlap) and a Hanning window to reduce any spectral leakage. This results in a frequency resolution of 2.44 Hz (0.015 BPF). The pre-multiplied spectra are presented in figure 6 for three heights and both ground stand-off distances. All energy spectra are dominated with a broadband hump at lower frequencies compared to the BPF. Particularly, in figure 6(a), which is extracted close to the stagnation point near the ground, the fluctuations are energetic at frequencies one to two orders of magnitude lower than the BPF. Higher up within the fountain, towards $z/R = 1.0$ and $z/R = 2.2$ (figures 6b and 6c, respectively), the energy distribution shifts towards slightly higher frequencies by the increase in turbulent fluctuations after the collision of
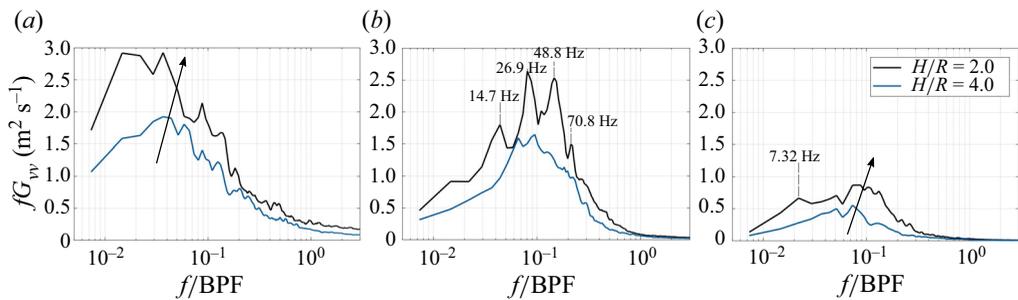
Figure 6. *Pre-multiplied energy spectra of the lateral velocity fluctuations in the centre of the fountain flow, for H/R = 2 and H/R = 4, and at heights of (a) z/R = 0.2, (b) z/R = 1.0 and (c) z/R = 2.2.*

the two opposing wall jets. As discussed in § 3.2, the intensity of the velocity fluctuations increases when re-ingestion takes place (indicated by the arrows in figure 6).

Furthermore, the spectra corresponding to $H/R = 4$ are relatively smooth in comparison with the spectra from the case of $H/R = 2$. The latter comprises distinct peaks at multiples of approximately 7 Hz in figure 6(*b*), thus indicating that the flow unsteadiness for the $H/R = 2$ case is distinctly different. The occurrence of these spectral peaks is later shown to be related to the re-ingestion switching of the fountain flow.

3.4. Re-ingestion switching cycle and time scale

After having shown the occurrence of a low-frequency unsteadiness in the fountain flow structure, the time-resolved flow field will aid in identifying the spatial–temporal dynamics of this unsteadiness. For the case of $H/R = 2$, re-ingestion occurs at certain time instances (recall figure 3 and its discussion), while other time instances are characterized by the absence of re-ingestion. During these latter instances, the fountain can occasionally reach locations significantly higher than the rotor height. Two sequences in figures 7(*a–d*) and 7(*e–h*) show these two different scenarios using sliding averaged results. The length of each sequence is 113 ms, corresponding to an approximate frequency of 8.8 Hz, comparable with the frequency at which the dominant flow fluctuations were identified in § 3.3.

The sequence in figure 7(*a–d*) starting at t_1 captures a relatively stable fountain flow reaching above the rotor disks. Hence, the phenomenon of fountain flow re-ingestion, by one of the two rotors, is minimal. Contrary to this is the statistically independent time sequence starting at t_2, shown in figure 7(*e–h*). In the first frame, the fountain leans towards the right rotor, where re-ingestion takes place at point A. At $t_2 + 38$ ms, this results in an increase in momentum at point B and the fountain directs towards the left rotor (see point C). In the subsequent frame $t_2 + 75$ ms, re-ingestion takes place in point D and more momentum towards the centre of the wake is found in point E. Finally, the fountain re-orientates back towards the right rotor, visible in point F. Within a full measurement acquisition period, several similarly looking switching cycles were observed.

The occurrence of the two different flow states described above (fountain flow eruption above the rotor disk and re-ingestion switching) closely resembles a 'bimodal' behaviour of a fountain flow associated with impinging, twin jets (Saddington et al., 2005; Stahl et al., 2021) and is suggested to be caused by the orientation of vortical structures in the turbulent wall jet (Stahl et al., 2021). On that note, the re-ingestion switching cycle as illustrated in figure 7(*e–h*) is not present for each sequence investigated along the measurement. Although not shown here for brevity, intermittent intervals of stable re-ingestion to either rotor are also present. On average, this happens more often for rotor 1 compared with rotor 2, which causes the slight inclination of the fountain to rotor 1 when computing the time-averaged results of figure 4. Given the unstable nature of the fountain and the low-Reynolds-number regime in which the rotor blades are operated, the bias is expected to be caused by minor discrepancies
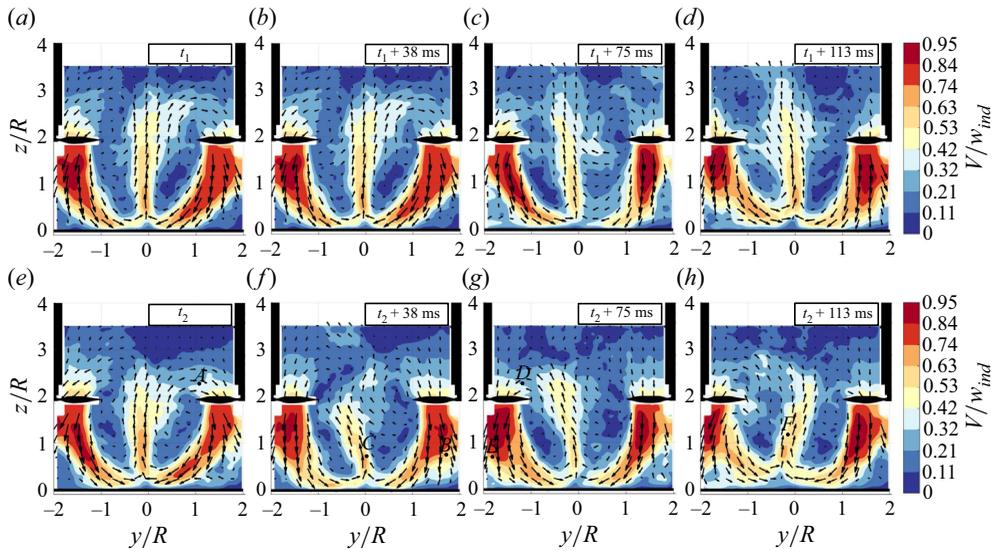
Figure 7. *Normalized velocity magnitude contours V/w_{ind} and 2-D velocity vectors of two time sequences of sliding averages (ensembles of 100 samples/0.25 s), with a temporal increment of $dt = 0.0375$ s. The series (a–d) is statistically independent from the series (e–h), with $t_2 = t_1 + 1.7$ s.*

in the geometrical/performance parameters between the two rotors. Nonetheless, re-ingestion is still seen to switch along the loop presented in figure 7(*e–h*) during the majority of the acquisition period. To quantify the re-ingestion switching, a time scale can be assigned for the case of $H/R = 2$. By following a particle trajectory during re-ingestion, the reciprocal of its velocity is integrated along a path s to compute the convective flow-around time. Note that the velocity $V(s)$ and trajectory length s depend on the system parameters of ground stand-off distance H and rotor thrust T. The resultant flow-around time is approximately $T_{conv} \approx 0.1$ s and corresponds to a frequency of $f_{conv} = 1/T_{conv} \approx 10$ Hz. This value is of the same order as the energy content at 7 Hz (and multiples of that) within the spectra of the lateral velocity fluctuations (figure 6). Furthermore, the flow-around time is representative of the fountain switching to the other rotor and back (see figure 7). Note that the velocity $V(s)$ and trajectory length s depend on the system parameters of ground stand-off distance H and rotor thrust T. Hence, for a given ground stand-off distance, and therefore constant trajectory length s, the convective frequency f_{conv} is expected to increase with an enhancement of the thrust.

Next, the cycle of re-ingestion switching is explored in further detail in §§ 4 and 5, with a modal analysis to identify its underlying spatial–temporal flow structures.

4. Modal decomposition of the unsteady flow field

It has now been established that the fountain flow re-ingestion can cause a dynamic cycle of switching. The goal is now to identify the energetic dynamic features that sustain this cycle. This is achieved through a reduced-order POD analysis. The low-order flow-field representation is presented in this section, and is used in § 5.2 to formulate a dynamic flow description of the re-ingestion switching cycle.

4.1. Application of classical POD

A POD decomposition is performed using data corresponding to all six acquisition periods for the condition of $H/R = 2$. Thus, the total space–time data consist of $m \approx 65\,000$ temporal snapshots, corresponding to roughly 16 s of data. Spatially, the data of the full field of view are employed. For the

POD, the formulation of Lumley (1967) is adopted, known as the classical POD (reviewed by Berkooz, Holmes, & Lumley, 1993). Considering that the amount of snapshots m exceeds the spatial rank of the data ($n \approx 40\,000$), the classical approach is favoured so that ensemble averaging in time can be performed (e.g. George, 1988; Tinney, Shipman, & Panickar, 2020). The decomposition deals with the velocity fluctuations only, computed as

$$\boldsymbol{u}'(\boldsymbol{x}, t) = \boldsymbol{u}(\boldsymbol{x}, t) - \bar{\boldsymbol{u}}(\boldsymbol{x}), \quad t = t_1, t_2, \ldots, t_m. \tag{4.1}$$

The velocity fluctuations are decomposed in a set of temporal coefficients, $a_i(t)$, and spatial modes, $\boldsymbol{\phi}_i(\boldsymbol{x})$, where i is the mode number. A full reconstruction of a single instantaneous field, using all n POD modes, is then generated through

$$\boldsymbol{u}'(\boldsymbol{x}, t) = \sum_{i=1}^{n} a_i(t) \boldsymbol{\phi}_i(\boldsymbol{x}). \tag{4.2}$$

In order to solve for the POD modes and temporal coefficients, an eigenvalue problem is constructed with the spatial modes $\boldsymbol{\phi}_i(\boldsymbol{x})$ defined as the eigenvectors of the covariance matrix, or two-point correlation tensor, $\boldsymbol{R}$, following

$$\boldsymbol{R}\boldsymbol{\phi}_i = \lambda_i \boldsymbol{\phi}_i, \quad \lambda_1 \geq \cdots \geq \lambda_n. \tag{4.3}$$

The covariance matrix $\boldsymbol{R}$ is generated using ensemble-averaging in time, following

$$\boldsymbol{R} = \langle \boldsymbol{u}'(\boldsymbol{x}, t) \boldsymbol{u}'(\boldsymbol{x}'', t) \rangle, \tag{4.4}$$

where the double prime is used to denote separations in space. In (4.3), λ_i denotes an ordered sequence of eigenvalues. By indicating the total resolved kinetic energy with E, equal to the sum of the eigenvalues, the relative energy fraction of each spatial mode $\boldsymbol{\phi}_i$ is equal to

$$\tilde{\lambda}_i = \frac{\lambda_i}{\sum_{k=1}^{n} \lambda_k} = \frac{\lambda_i}{E}. \tag{4.5}$$

Finally, the temporal coefficients $a_i(t)$ can be computed by projecting the original data on the spatial modes, according to

$$a_i(t) = \int \boldsymbol{u}'(\boldsymbol{x}, t) \boldsymbol{\phi}_i(\boldsymbol{x}) \, \mathrm{d}\boldsymbol{x}. \tag{4.6}$$

4.2. Energy distribution and spatial POD mode shapes

Data reduction using the spatial POD ranks the modes according to their relative energy contribution to the total resolved energy in the flow domain. Figure 8 presents the relative energy fraction and cumulative energy for each mode. The system is relatively low-dimensional, given that 70 % of the total resolved energy is captured in less than 100 modes. The energy fractions of the first five modes are 7.0 %, 4.8 %, 4.3 %, 3.9 % and 3.3 %, respectively.

Figure 9 presents the first five POD mode shapes, split by their lateral and axial velocities. A sketch is included in figure 9(c) to show the contribution of each mode to the time-averaged flow field by highlighting the primary flow features. We now proceed with a brief discussion of each mode.

In the discussion of figure 7(a–d), an intermittent appearance of the fountain rising above the rotor disk was identified. Since no re-ingestion takes place in that case, the flow field is relatively symmetric with a large vertical velocity magnitude between/above the rotors. Mode 1 in figure 9 is representative of this flow state. A sideways inclination of the fountain is captured by mode 2 and predominantly shows activity below the rotor disk. When the associated temporal coefficient would decrease from a positive
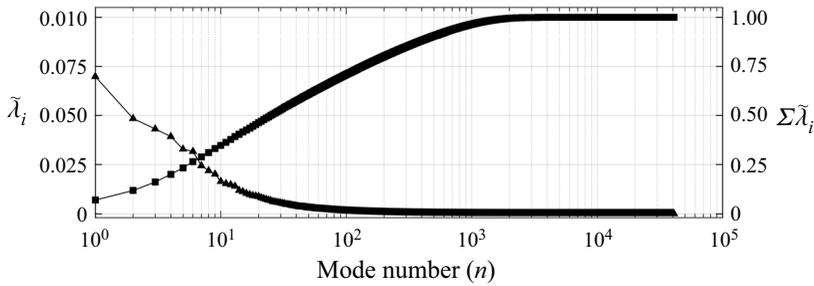
Figure 8. *Energy fraction and cumulative energy as a function of POD mode number n.*

value to a negative one, the fountain will change inclination from the left rotor to the right. There is also an activity in the axial direction near the wall, showing a relation with the two toroidal separation regions. These two regions simultaneously grow/shrink in size. Similar to mode 1, mode 3 comprises an asymmetric mode shape. Here, most of the energy is contained at the inflow and toroidal separation region of rotor 1. Again, as for mode 2, we see an increase of the separation regions below rotor 1 when re-ingestion goes to the other rotor. Mode 4 contains most of the activity in the axial motions within the separation regions. These motions have opposite sign for the regions associated with rotors 1 and 2, e.g. one separation region grows while the other one shrinks, and vice versa. Finally, mode 5 represents a lateral drifting of the entire fountain column, where a positive time coefficient is associated with the fountain being closer to the left rotor. When time is retained in the analysis, the zero-mean temporal coefficient of each POD mode signifies the degree of activity of the mode, during the measurement time. Temporal coefficients are analysed next to show the dynamic behaviour and mode coupling.

4.3. Temporal POD coefficients

The temporal coefficients are inferred from projecting the raw data back on the POD modes. Recall that six different acquisition periods were used to compute the POD modes. Hence, the corresponding time coefficient of each mode consist of six independent segments, which are presented in figures 10(*a*) and 10(*b*) for modes 1 and 2, respectively.

A simple visual inspection of the a_1 and a_2 time series in figures 10(*a*) and 10(*b*) already reveals that mode 1 resides at a lower frequency in comparison with mode 2. This is further explored by computing the energy spectra of the temporal mode coefficients. Pre-multiplied energy spectra, normalized with the resolved energy per mode, are shown in figure 10(*c*) for both modes 1 and 3 and in figure 10(*d*) for modes 2, 4 and 5. All spectra were computed with ensemble averaging each of the six segments of data, of which each segment itself was first split into bins of 2^{11} samples long (yielding a spectral resolution of d$f \approx 2$ Hz). Note that the abscissa has been normalized with the convective frequency: $f^* = f/f_{conv}$ (see § 3.4).

Overall, the energy content resides at low frequencies compared with the BPF, as was already noted in the spectra of the raw, lateral velocity fluctuations presented in figure 6. Most interestingly, modes 2, 4 and 5 comprise a similar spectral distribution, concentrated around the convective frequency. This indicates that these modes are linked to the flow recirculation cycle. The coupling between these three modes is investigated in § 5 through a more detailed analysis of the temporal coefficients.

5. Dynamic flow description

Having identified the re-ingestion switching in § 3.4, here a physical description of this cycle and its underlying features is presented. This starts with an analysis on the coupling between the modes that describe this mechanism.
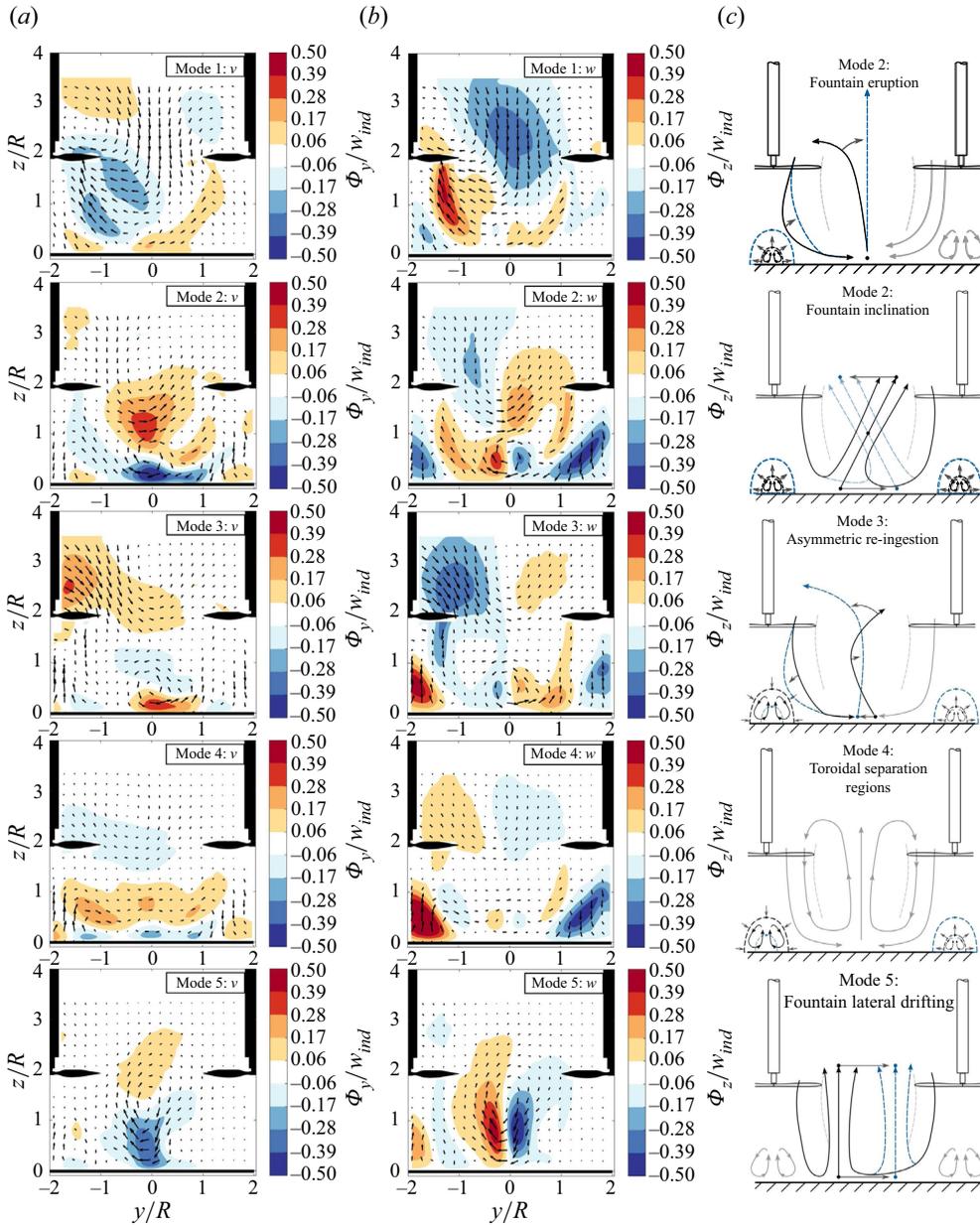
Figure 9. *The POD mode shapes: (a) v and (b) w component. (c) The contribution of the mode to the flow field when the time coefficient decays from positive unity (black streamlines) to negative unity (blue streamlines).*

5.1. Modal coupling

The temporal coupling between modes 2, 4 and 5 is first confirmed by plotting a magnitude of the linear coherence for every combination of two temporal mode coefficients in the range $n = 1$ to 6. First, the linear coherence was computed between temporal coefficients a_i and a_j, following

$$\gamma^2(f) = \frac{|G_{a_i a_j}(f)|^2}{G_{a_i a_i}(f) G_{a_j a_j}(f)}. \tag{5.1}$$
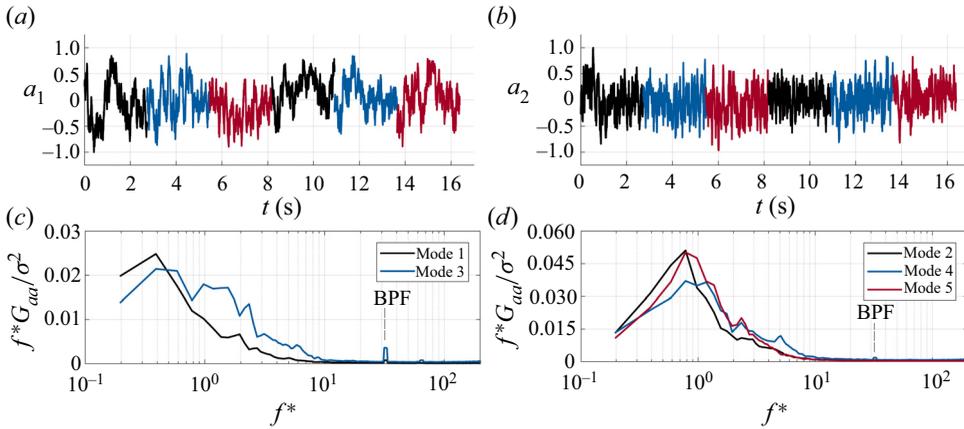
Figure 10. *Temporal POD coefficient of (a) mode 1, a_1, and (b) mode 2, a_2. Pre-multiplied energy spectra of the temporal coefficients of (c) modes 1 and 3 and (d) modes 2, 4 and 5. The frequency has been normalized by the convective frequency, i.e. $f^* = f/f_{conv}$.*
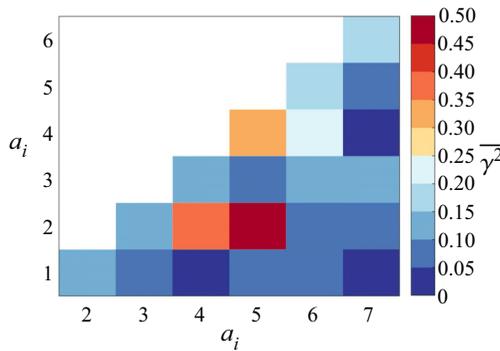
Figure 11. *Coherence magnitude $\overline{\gamma^2}$ for combinations of temporal mode coefficients, taken as the average coherence value over $0.75f_{conv} \leq f \leq 1.25f_{conv}$.*

Here $G_{a_i a_i}(f)$ is the energy spectrum of temporal coefficient $a_i(t)$ and $G_{a_i a_j}(f)$ is the cross-spectrum of mode coefficients $a_i(t)$ and $a_j(t)$. The spectral coherence is calculated using windows of 2^{11} samples, similar to how the energy spectra of figure 10 were generated. The coherence indicates the fraction of energy corresponding to the coherent fluctuations in $a_i(t)$ and $a_j(t)$; note that γ^2 is a normalized quantity, thus $0 \leq \gamma^2 \leq 1$. When averaging γ^2 over a frequency domain of interest, that is, the rate of the re-ingestion switching loop ($0.75f_{conv} \leq f \leq 1.25f_{conv}$), the resultant magnitude $\overline{\gamma^2}$ is obtained and its amplitude is plotted in figure 11. Here, coherence values between 0.3 and 0.5 are found across the convective frequency domain for the coupling between modes 2, 4 and 5. The coherence magnitudes between the other mode combinations remain below 0.25.

The relation between modes 2, 4 and 5 is further examined in the time domain by computing the cross-correlation between each of the temporal coefficients of these modes. The results in figure 12(a) show a correlation and anti-correlation peak in the proximity of a lag of $\tau = 0$ s. The zoomed-in plot of figure 12(b) reveals a similar shape of the cross-correlation signal for each of the three mode combinations. First of all, this is characterized by a correlation value of approximately 0.3 at a positive lag, indicated by τ_i. Second, by the orthogonality definition in the modal decomposition, a zero correlation value for $\tau = 0$ s is found. Finally, a weaker but present anti-correlation value is visible at a negative lag, i.e. $\tau < 0$.
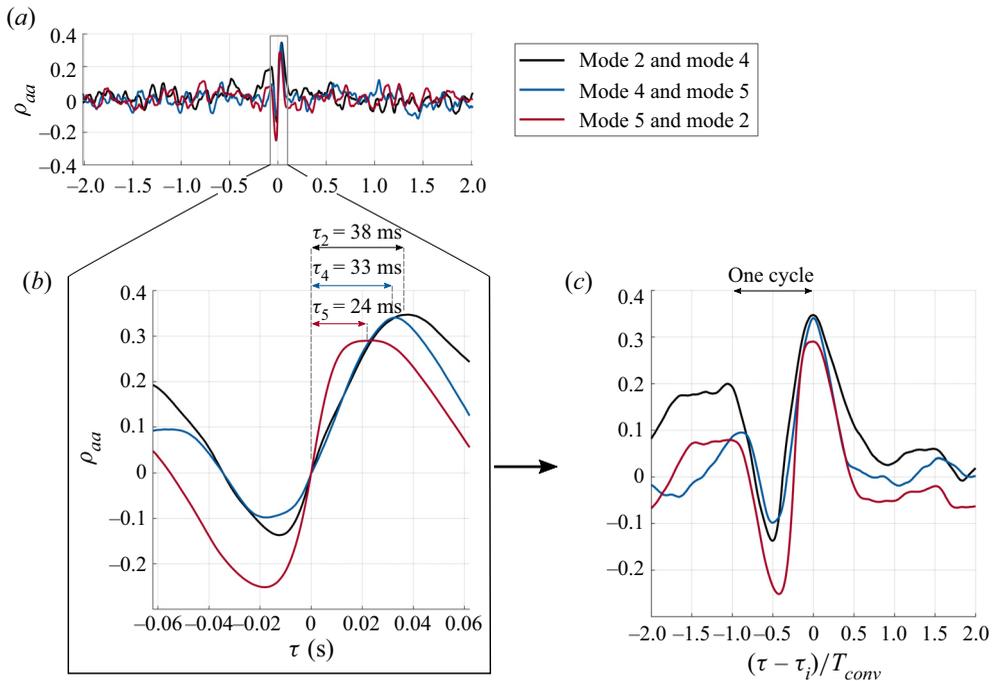
Figure 12. *(a) Overview and (b) zoomed-in plot of the temporal cross-correlation coefficient, and corresponding lags for modes 2, 4 and 5. (c) Same as (a,b) but subtraction of lags in (b) and normalization of lag τ by T_{conv}.*

The sum of the lags τ_i, effectively creating a loop from mode 2 back to 2 while passing modes 4 and 5, closely resembles the flow-around time introduced in § 3.4, i.e. $\sum \tau_i = 94$ ms $\approx T_{conv}$. Hence, these modes represent successive, energetic events that occur along the re-ingestion cycle. This apparent cyclic behaviour is also confirmed by translation of the cross-correlation signals. By subtracting the lag τ_i from figure 12(b) and normalizing τ by the flow-around time T_{conv} (resulting in figure 12(c). The anti-correlation of each of the mode combinations is now shifted towards a value of 0.5. Moreover, a second positive correlation peak also becomes apparent for a lag value of -1, indicating similar behaviour between the modes which is a complete cycle ahead of the dominant correlation peak. The physical interpretation of the combination of modes 2, 4 and 5 and the meaning of their relative lag τ_i will become clear from a low-order reconstruction presented next.
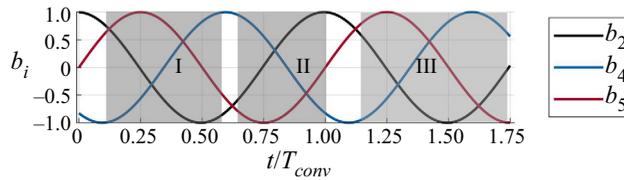
5.2. Low-order reconstruction

The reduced-order flow with its energetic features will allow for a description of dynamic flow features that are a part of establishing the cycle of re-ingestion switching. The coupling between these modes is reconstructed using a pseudo time coefficient b_i, based on a harmonic wave of frequency f_{conv}, over a time interval of $0 \leq t \leq 1.75T_{conv}$, following

$$b_i = \sin(2\pi f_{conv} t + \psi_i), \quad 0 \leq t \leq 1.75T_{conv}. \tag{5.2}$$

Here the relative phase offset ψ_i between the time coefficients b_i is based on the sum of the cross-correlation lag τ_i between the modes:

$$\psi_i = 2\pi f_{conv} \sum_i \tau_i, \quad i \in \{2, 4, 5\}. \tag{5.3}$$

Figure 13. *Pseudo time coefficients b_i used for the low-order reconstruction. Intervals I, II and III indicate the time domains for velocity field reconstructions in figures 14(a), 14(b) and 14(c), respectively.*

Figure 13 presents the adapted time coefficients b_i computed from (5.2). The original temporal coefficients a_i, derived directly from the time-resolved velocity field, have a different shape from what is presented in figure 13. However, the purpose of using the pseudo time coefficients b_i is to show how the modes statistically combine during the flow re-ingestion cycle.

Sticking to the temporal simplification of harmonic waves, the velocity field can be reconstructed by the sum of the spatial modes 2, 4 and 5, multiplied by their corresponding time coefficient b_i, so that

$$\hat{u}(x, t) = \bar{u}(x) + \sum_i b_i(t)\phi_i(x), \quad i \in \{2, 4, 5\}. \tag{5.4}$$

By examining the reconstructed velocity field $\hat{u}$, three successive events can be identified within the trajectory of re-ingestion. These events are investigated independently by the definition of spatial and temporal subdomains in the reconstructed velocity field $\hat{u}$, denoted by I, II and III. These time interval are highlighted by the grey zones in figure 13. The spatial subdomains of I, II and III are based on a trajectory of re-ingestion to rotor 1, which is split into three parts. These spatial subdomains, alongside the corresponding time series of the reconstructed velocity field $\hat{u}$, are presented in figure 14.

The three sequential events of figure 14(a–c) present the core mechanism of the flapping of the fountain and the re-ingestion switching. Subdomain I, illustrated in figure 14(a), shows three successive snapshots. The first of which, at $t/T_{conv} = 0.11$, presents the emerging fountain from the ground with an inclination towards the left. The fountain is then convected upwards and re-ingested into rotor 1 in the final snapshot at $t/T_{conv} = 0.58$. After re-ingestion, the momentum in the slipstream increases, as shown in figure 14(b). Stagnation in the centre of the slipstream, as indicated in the left snapshot, is removed and an attachment of the wake to the ground positions itself laterally below the rotor axis, at $t/T_{conv} = 1.00$. With more lateral momentum in the wall jet, the foot of the fountain drifts towards the right (see figure 14c). After this, ejection from the ground is inclined towards the right rotor, and the cycle is repeated in mirrored orientation. Each of the three events in figure 14 also resembles the results of the time-resolved flow-field analysis in figure 7.

One should note that, by the bias of the time-averaged flow field, the cycle of re-ingestion towards the right rotor is less pronounced. However, the same dynamic features are present. Moreover, as noted in § 3.4, intervals of stable re-ingestion to either rotor are also found, which means that re-ingestion does not switch after every flow-around cycle. During these intervals, the stronger wall jet is not able to push the foot of the fountain far enough towards the other rotor for the switch to occur. For completeness, the re-ingestion switching cycle, along with the corresponding (statistical) delays between the events, are schematically represented in figure 15.

In the schematic of the re-ingestion loop of figure 15, the first three events show the observations as seen in figures 14(a) and 14(b). In the fourth event of figure 15, the fountain is seen to drift towards the right, as seen by the middle snapshot in figure 14(c). This completes the loop after a time delay of T_{conv} from the first event. After this follow two possibilities: either the cycle is repeated with the same orientation but with a more pronounced inclination of the fountain, or the stagnation point has drifted far enough to the subsequent rotor to allow the re-ingestion to switch, effectively repeating the loop in mirrored orientation.
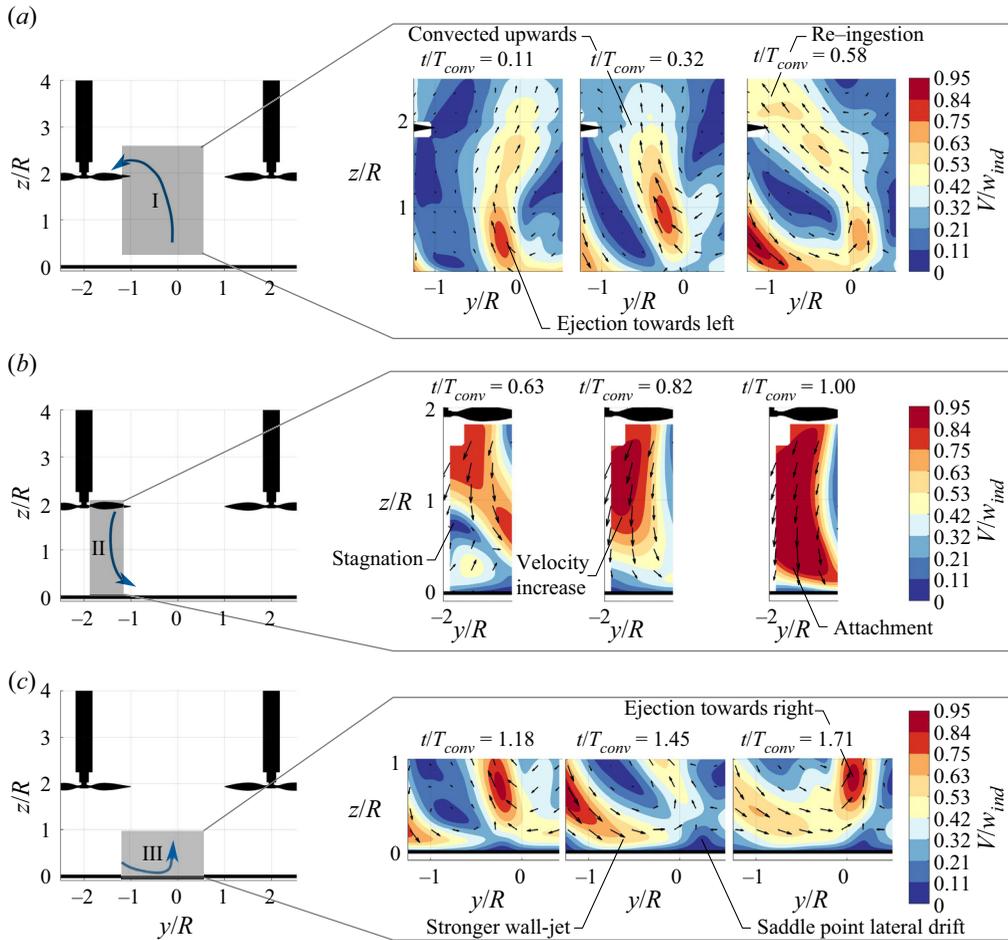
Figure 14. *Normalized velocity magnitude contours V/w_{ind} of the reconstructed velocity field $\hat{u}$, visualized along the trajectory of re-ingestion to highlight successive critical events. (a) Convection of ejected structures to the inflow of rotor 1, (b) dynamic pressure increase in the wake and (c) lateral drifting of the saddle point. The left-hand plots in (a–c) illustrate the spatial domain, based on the trajectory of re-ingestion (blue arrow), corresponding to the time intervals of figure 13.*
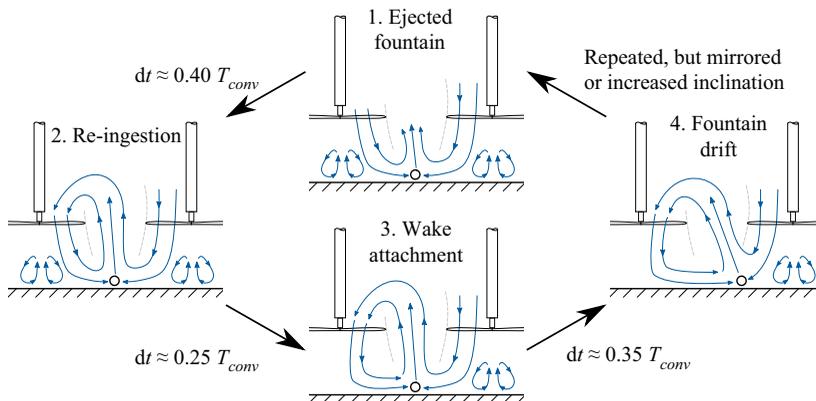
Figure 15. *Schematic representation of events during the re-ingestion of the fountain column.*

6. Conclusion

The unsteady flow field associated with a two-rotor system in ground proximity has been investigated experimentally. Findings presented cover the understanding of the unsteady interactions of rotorcraft during vertical take-off and landing. Coherent structures are shown to be ejected from the ground in the fountain. For lower ground stand-off distances, these structures rise above the rotor disks where they are re-ingested into one of the two rotors. During the re-ingestion, velocity fluctuations are increased in the fountain, resulting in more pronounced side-by-side drifting of the column. These dynamic features are observed at an intermittent frequency, which is related to the convective frequency of the re-ingestion loop. Consequently, this intermittent frequency depends on the system parameters (ground stand-off distance and rotor thrust) through the height of the fountain and its characteristic velocity.

Different dynamic features of fountain inclination, toroidal separation regions and fountain lateral drifting are returned as individual POD modes and responsible for establishing the cycle of re-ingestion switching. These POD modes are coupled with a statistical delay. A reconstruction with only the few relevant modes shows that when the fountain is inclined towards one of the rotors, a non-axial inflow condition is created in which more momentum is transferred to the centre of the rotor slipstream. Consequently, the wake does not separate in the centre of the wake close to the ground but attaches to the wall. With more lateral momentum in the wall jet, the fountain drifts towards the subsequent rotor. After this, the re-ingestion either switches towards the other rotor or is maintained to the same rotor with a shallower angle.

A second regime of the fountain is also present along certain time intervals, with reduced lateral fluctuations. Here, the fountain emerges vertically from the ground and re-ingestion is minimized. This apparent bimodal behaviour is similar to observations of twin impinging jets, indicating a relationship with the orientation of the coherent structures in the turbulent wall jet.

The aforementioned dynamic features associated with multi-rotor vehicles in ground operations can cause fluctuations in thrust at frequencies of two orders of magnitude lower than the BPF, which can be detrimental to controllability. Moreover, by the unsteady loading on the blades, and the ingestion of the coherent structures originating from the fountain, the acoustic footprint of these systems is expected to increase as they approach the ground.

Author contributions. H.N.J.D. – conceptualization; data acquisition; methodology; investigation; visualization; writing; W.J.B. – conceptualization; methodology; investigation; writing; supervision; F.S. – conceptualization; methodology; writing; supervision; M.T. – funding acquisition; methodology; writing; supervision; D.R. – funding acquisition; conceptualization; methodology; investigation; writing; supervision.

References

Berkooz, G., Holmes, P., & Lumley, J.L. (1993). The proper orthogonal decomposition in the analysis of turbulent flows. *Annual Review of Fluid Mechanics*, *25*(1), 539–575.

Cabrita, P.M., Saddington, A.J., & Knowles, K. (2005). PIV measurements in a twin-jet STOVL fountain flow. *The Aeronautical Journal*, *109*(1100), 439–449.

Cheeseman, I., & Bennett, W. (1955). *The effect of the ground on a helicopter rotor in forward flight* (Aeronautical Research Council TR 3021).

Conyers, S.A., Rutherford, M.J., & Valavanis, K.P. (2018). *An empirical evaluation of ground effect for small-scale rotorcraft*. In *2018 IEEE international conference on robotics and automation (ICRA)* (pp. 1244–1250). New York, NY: Institute of Electrical and Electronics Engineers.

Dekker, H.N.J., Ragni, D., Baars, W.J., Scarano, F., & Tuinstra, M. (2022). Aerodynamic interactions of side-by-side rotors in ground proximity. *AIAA Journal*, *60*(7), 4267–4277.

Faleiros, D.E., Tuinstra, M., Sciacchitano, A., & Scarano, F. (2019). Generation and control of helium-filled soap bubbles for PIV. *Experiments in Fluids*, *60*(3), 1–17.

Fradenburgh, E.A. (1960). The helicopter and the ground effect machine. *Journal of the American Helicopter Society*, *5*(4), 24–33.

Garrow, L.A., German, B.J., & Leonard, C.E. (2021). Urban air mobility: A comprehensive review and comparative analysis with autonomous and electric ground transportation for informing future research. *Transportation Research Part C: Emerging Technologies*, *132*, 103377.

George, W.K. (1988). Insight into the dynamics of coherent structures from a proper orthogonal decomposition. In S. Kline (Ed.), *The structure of near wall turbulence*, Proceedings of symposium on near wall turbulence, Dubrovnik, Yugoslavia, 16–20 May 1988 (pp. 168–180). New York, NY: Hemisphere.

He, X., & Leang, K.K. (2020). Quasi-steady in-ground-effect model for single and multirotor aerial vehicles. *AIAA Journal*, *58*(12), 5318–5331.

Healy, R., McCauley, J., Gandhi, F., Sahni, O., & Mistry, M. (2021). A computational investigation of side-by-side rotors in ground effect. In *Proceedings of the 77th VFS annual forum (virtual)*. Vertical Flight Society.

Huang, L., & El-Genk, M.S. (1994). Heat transfer of an impinging jet on a flat surface. *International Journal of Heat and Mass Transfer*, *37*(13), 1915–1923.

Jeon, Y.J., Müller, M., Michaelis, D., & Wieneke, B. (2018). Efficient reconstruction of flow field with pressure from particle tracks: VIC. *Bulletin of the American physical society*, 63(13), BAPS.2018.DFD.M30.8. Retrieved from http://meetings.aps.org/link/BAPS.2018.DFD.M30.8

Lee, T.E., Leishman, J.G., & Ramasamy, M. (2010). Fluid dynamics of interacting blade tip vortices with a ground plane. *Journal of the American Helicopter Society*, *55*(2), 57–92.

Lumley, J.L. (1967). The structure of inhomogeneous turbulent flows. In A.M. Yaglom & V.I. Tatarsky (Eds.), *Atmospheric turbulence and radio wave propagation* (pp. 166–176). Moscow, Russia: Publishing House Nauka.

Maisel, M., Giulanetti, D.J., & Dugan, D.C. (2000). *The history of the XV-15 tilt rotor research aircraft: From concept to flight* (No. 17). National Aeronautics and Space Administration, Office of Policy and Plans, NASA History Division.

Milluzzo, J.I., III, & Leishman, J.G. (2017). Vortical sheet behavior in the wake of a rotor in ground effect. *AIAA Journal*, *55*(1), 24.

Nathan, N., & Green, R. (2012). The flow around a model helicopter main rotor in ground effect. *Experiments in Fluids*, *52*(1), 151–166.

Polak, D.R., & George, A.R. (1998). Flowfield and acoustic measurements from a model tiltrotor in hover. *Journal of Aircraft*, *35*(6), 921–929.

Polak, D.R., Rehm, W., & George, A.R. (2000). Effects of an image plane on the tiltrotor fountain flow. *Journal of the American Helicopter Society*, *45*(2), 90–96.

Potsdam, M.A., & Strawn, R.C. (2005). CFD simulations of tiltrotor configurations in hover. *Journal of the American Helicopter Society*, *50*(1), 82–94.

Rizzi, S.A., Huff, D.L., Boyd, D.D., Bent, P., Henderson, B.S., Pascioni, K.A., . . . Snider, R. (2020). *Urban air mobility noise: Current practice, gaps, and recommendations* (No. NASA/TP-20205007433).

Saddington, A.J., Cabrita, P., & Knowles, K. (2005). Large-scale instabilities in a STOVL upwash fountain. In *Engineering turbulence modelling and experiments* (pp. 667–676). New York, NY: Elsevier.

Sanchez-Cuevas, P., Heredia, G., & Ollero, A. (2017, August). Characterization of the aerodynamic ground effect and its influence in multirotor control. *International Journal of Aerospace Engineering*, *2017*, 1–17.

Schanz, D., Gesemann, S., & Schröder, A. (2016). Shake-the-box: Lagrangian particle tracking at high particle image densities. *Experiments in Fluids*, *57*(5), 1–27.

Schneiders, J.F., & Scarano, F. (2016). Dense velocity reconstruction from tomographic PTV with material derivatives. *Experiments in Fluids*, *57*(9), 1–22.

Siclari, M.J., Migdal, D., Luzzi, T.W., Jr., Barche, J., & Palcza, J.L. (1976). Development of theoretical models for jet-induced effects on V/STOL aircraft. *Journal of Aircraft*, *13*(12), 938–944.

Stahl, S.L., Prasad, C., & Gaitonde, D.V. (2021). Distinctions between single and twin impinging jet dynamics. *The Journal of the Acoustical Society of America*, *150*(2), 734–744.

Thipphavong, D.P., Apaza, R., Barmore, B., Battiste, V., Burian, B., Dao, Q., . . . Verma, S.A. (2018). Urban air mobility airspace integration concepts and considerations. In *2018 aviation technology, integration, and operations conference, June 2018* (AIAA Paper 2018-3676). American Institute of Aeronautics and Astronautics.

Tinney, C.E., Shipman, J., & Panickar, P. (2020). Proper-orthogonal-decomposition-based reduced-order models for characterizing ship airwake interactions. *AIAA Journal*, *58*(2), 633–646.

Weitsman, D., Stephenson, J.H., & Zawodny, N.S. (2020). Effects of flow recirculation on acoustic and dynamic measurements of rotary-wing systems operating in closed anechoic chambers. *The Journal of the Acoustical Society of America*, *148*(3), 1325–1336.

Wieneke, B. (2015). PIV uncertainty quantification from correlation statistics. *Measurement Science and Technology*, *26*(7), 074002.

Wojno, J.P., Mueller, T.J., & Blake, W.K. (2002). Turbulence ingestion noise, part 1: Experimental characterization of grid-generated turbulence. *AIAA Journal*, *40*(1), 16–25.

Zanotti, A., Savino, A., Palazzi, M., Tugnoli, M., & Muscarello, V. (2021). Assessment of a mid-fidelity numerical approach for the investigation of tiltrotor aerodynamics. *Applied Sciences*, *11*(8), 3385.

Zhou, W., Ning, Z., Li, H., & Hu, H. (2017). An experimental investigation on rotor-to-rotor interactions of small UAV propellers. In *35th AIAA applied aerodynamics conference* (AIAA Paper 2017–3744). American Institute of Aeronautics and Astronautics.